Nanoscale Advances

ROYAL SOCIETY OF CHEMISTRY

PAPER

View Article Online
View Journal | View Issue

Check for updates

Cite this: *Nanoscale Adv.*, 2022, **4**, 2288

Enhanced electrocatalytic reduction of CO_2 to formate *via* doping Ce in Bi_2O_3 nanosheets†

Xiao Li,‡[a] Ningkang Qian,‡[a] Liang Ji,[a] Xingqiao Wu,[a] Junjie Li,[a] Jingbo Huang,[a] Yucong Yan,[ac] Deren Yang [a] and Hui Zhang *[ab]

Received 3rd March 2022
Accepted 28th March 2022

DOI: 10.1039/d2na00141a

rsc.li/nanoscale-advances

Formate is considered as the most economically viable product of the prevalent electrochemical CO_2 reduction (ECR) products. However, most of the catalysts for ECR to formate in aqueous solution often suffer from low activity and limited selectivity. Herein, we report a novel Ce-doped Bi_2O_3 nanosheet (NS) electrocatalyst by a facile solvothermal method for highly efficient ECR to formate. The 5.04% Ce-doped Bi_2O_3 NSs exhibited a current density of 37.4 mA cm^{-2} for the production of formate with a high formate faradaic efficiency (FE) of 95.8% at −1.12 V. The formate FE was stably maintained at about 90% in a wide potential range from −0.82 to −1.22 V. More importantly, density functional theory (DFT) calculations revealed that Ce doping can lead to a significant synergistic effect, which promotes the formation and the adsorption of the OCHO* intermediate for ECR, while significantly inhibiting the hydrogen evolution reaction *via* depressing the formation of *H, thus helping achieve high current density and FE. This work provides an effective and promising strategy to develop efficient electrocatalysts with heteroatom doping and new insights for boosting ECR into formate.

Introduction

Nowadays, excessive CO_2 emission has caused many severe problems related to the resources, environment, and climate, known as the "greenhouse effect".[1] Therefore, besides reducing CO_2 production, converting CO_2 into fuels or value-added chemicals seems to be necessary, which is also an urgent focus of research.[2–5] There are several routes for the chemical conversion of CO_2, including thermochemical,[6] photochemical,[7] biochemical,[8] and electrochemical reactions.[9–11] Among these conversion approaches, electrochemical reduction of CO_2 powered by renewable energies is more attractive because it enables better sustainable development of energy and the environment. Nevertheless, some huge challenges remain in electrochemical CO_2 reduction (ECR) in aqueous media, such as the low activity, even when electrocatalysts and high electrode reduction potential are applied; the low selectivity, caused by the competitive hydrogen evolution reaction (HER); and low stability of catalysts.[12–14] Therefore, it's highly desired to develop efficient electrocatalysts for ECR.

Formate is viewed as the most economically viable product of the prevalent ECR products, and it is promising for energy and industrial related applications.[15–19] Recently, various metallic catalysts have proved to be effective to form formate (or HCOOH) through ECR.[20–24] Among these electrocatalysts explored to date, Bi-based materials have been widely investigated because of their low toxicity, earth-abundance, and high activity. However, various Bi-based electrocatalysts usually suffer from undesirable activity with a narrow potential window of high selectivity, a low current density for the formation of formate and relatively poor selectivity for formate production.[15,20,24–28] Up to now, a lot of effort has been devoted to improving the ECR performance of Bi-based electrocatalysts, such as tuning the size,[29] controlling the morphology,[25–28,30,31] and heterostructure engineering.[32–36] Among these strategies, element doping to regulate the electronic structure of catalysts has been regarded as a powerful way to enhance the activity of ECR. The introduction of heteroatoms (*e.g.* Sn, S, and B) can modify the electronic structures of the active sites and result in optimal adsorption energy of the reaction intermediates.[37–40] Cerium-based and ceria oxide-based catalysts are not ideal ECR electrocatalysts because of their poor intrinsic activity and the existence of the competitive HER. But some reports have proved that the activity of some ECR electrocatalysts can be effectively improved by combining with ceria through rational regulation.[41–45] Therefore, it is reasonable to expect that doping Ce in Bi-based oxide may improve the activity towards the ECR.

[a]*State Key Laboratory of Silicon Materials and School of Materials Science and Engineering, Zhejiang University, Hangzhou, Zhejiang 310027, People's Republic of China. E-mail: msezhanghui@zju.edu.cn*

[b]*Institute of Advanced Semiconductors, Hangzhou Innovation Center, Zhejiang University, Hangzhou, Zhejiang 310027, People's Republic of China*

[c]*BTR New Material Group CO., LTD, GuangMing District, Shenzhen 518106, People's Republic of China*

† Electronic supplementary information (ESI) available. See DOI: 10.1039/d2na00141a

‡ These authors contributed equally to this work

Herein, we report the facile synthesis of Ce-doped Bi_2O_3 nanosheets (NSs) *via* a facile solvothermal method. The obtained electrocatalysts showed a remarkable electrocatalytic activity for the production of formate through ECR in a CO_2-saturated 0.5 M $KHCO_3$ electrolyte in a H-cell. 5.04% Ce-doped Bi_2O_3 NSs show the highest faradaic efficiency (FE) (95.8%) with a current density of 37.4 mA cm^{-2} for formate at −1.12 V *versus* the reversible hydrogen electrode (RHE), which is better than those of undoped Bi_2O_3 NSs (89.1%, 26.6 mA cm^{-2}). This sample also possessed a wider negative potential range (from −0.82 to −1.22 V), in which the FE of formate was about 90%. Furthermore, 5.04% Ce-doped Bi_2O_3 NSs show a good catalytic stability over 10 h. Indeed, density functional theory (DFT) calculations suggest the mechanism for the enhancement in activity. Finally, we integrate 5.04% Ce-doped Bi_2O_3 NSs with a dimensionally stable anode (DSA) and achieve battery-driven CO_2/H_2O splitting to formate/O_2 with excellent activity.

Results and discussion

The Ce-doped Bi_2O_3 NSs and undoped Bi_2O_3 NSs were prepared in polyol media by a solvothermal method. The details of the synthetic procedure are shown in Experimental section.† X-ray diffraction (XRD) patterns (Fig. S1†) show that these four samples all display a crystalline phase of cubic Bi_2O_3 (JCPDS no. 27-0052), and four obvious diffraction peaks can be assigned to the (111), (200), (220) and (311) planes. There is no diffraction peak associated with CeO_2 or other types of Ce-based oxide to be observed in the XRD patterns, indicating that no Ce-based oxide coexists in Ce-doped Bi_2O_3 NSs. Moreover, the transmission electron microscopy (TEM) and high angle annular darkfield scanning transmission electron microscopy (HAADF-STEM) images show that the undoped Bi_2O_3 product exhibited a sheet-like nanostructure (Fig. S2a and b†). The high-resolution TEM (HRTEM) images (Fig. S2c†) of the undoped Bi_2O_3 NSs show a lattice spacing of about 0.276 nm that corresponds to the {200} facets of cubic Bi_2O_3. The HAADF-STEM-EDX images in Fig. S2d† demonstrate the uniform distribution of Bi and O elements in the undoped NSs. The sheet-like shape is well preserved after doping 5.04% atomic percentage of Ce in Bi_2O_3 NSs, as shown in the TEM (Fig. 1a) and HAADF-STEM (Fig. 1b) images. The HRTEM image of 5.04% Ce-doped Bi_2O_3 NSs in Fig. 1c shows the fringes with a lattice spacing of 0.278 nm that also corresponds to the {200} facets of Bi_2O_3. The expansion of the lattice fringes may result from the larger atomic radius of Ce compared with that of Bi. Additionally, elemental mapping images of 5.04% Ce-doped Bi_2O_3 NSs in Fig. 1d demonstrate that the Bi, Ce and O elements are uniformly distributed throughout the NSs without any element aggregation. Furthermore, the morphological, structural and compositional characterization of the 2.28% and 7.96% Ce-doped Bi_2O_3 NSs was also carried out (Fig. S3 and S4†). It should be noted that 2.28%, 5.04% and 7.96% represent the atomic percentage of Ce, and they were determined by using inductively coupled plasma atomic emission spectrometry (ICP-AES). The valence states of Bi and Ce were analyzed by X-ray photoelectron spectroscopy (XPS), as shown in Fig. S5 and S6.† The only two main peaks in the Bi 4f spectra (Fig. S6a, c, e, and g†) demonstrate a single oxidation state of Bi^{3+} for the undoped Bi_2O_3 NSs and three Ce-doped Bi_2O_3 NSs. The XPS spectra of Ce 3d (Fig. S6b, d, f, and h†) were fitted into 6 peaks corresponding to the Ce $3d_{5/2}$ and Ce $3d_{3/2}$ states. The V_0, U_0, V_1 and U_1 peaks are assigned to Ce^{4+} species, and the remaining two peaks are associated with Ce^{3+} species.[46] This result demonstrates that the valence states of Ce in Ce-doped Bi_2O_3 NSs are a mixture of Ce^{3+} and Ce^{4+} (the proportions of Ce^{3+} and Ce^{4+} are also shown in Fig. S6†).

To evaluate the catalytic properties of the Ce-doped Bi_2O_3 NSs including undoped Bi_2O_3 NSs toward CO_2 electroreduction, the electrocatalytic reactions are carried out in homemade H-type cells, and the linear sweep voltammetry (LSV) measurements are conducted in 0.5 M $KHCO_3$ at normal temperature and pressure. As shown in Fig. S7,† the negative current densities for these electrocatalysts in CO_2 are much higher than those in an Ar atmosphere, indicating their excellent intrinsic activities for reduction of CO_2 and a more favorable ECR activity over the competitive HER. To identify the reduction products and current densities at various potentials, the controlled potential electrolysis is carried out for the four electrocatalysts (Fig. S8†). The gas-phase products are detected using a gas chromatograph (GC), and the liquid products are quantitatively analyzed by ion chromatography (IC). Formate was measured by ion chromatography according to the standard curve (Fig. S9†). The summarized FEs of all products at various potentials in Fig. S10† demonstrate that formate is the only liquid product and also the predominant one among the whole CO_2 reduction products. As shown in Fig. 2a, the total negative current density (j_{total}) of Ce-doped Bi_2O_3 NSs remarkably increases compared with that of undoped Bi_2O_3 NSs. Among them, 5.04% Ce-doped

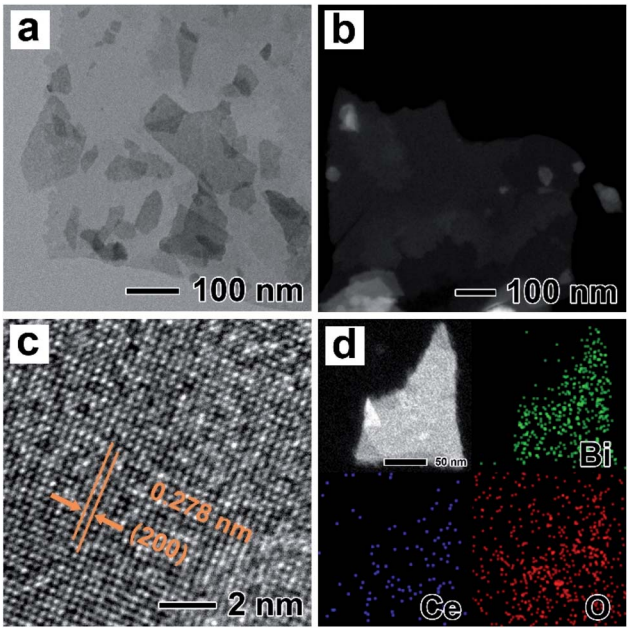

Fig. 1 (a) TEM, (b) HAADF-STEM, (c) HRTEM, and (d) elemental mapping images of 5.04% Ce-doped Bi_2O_3 NSs.

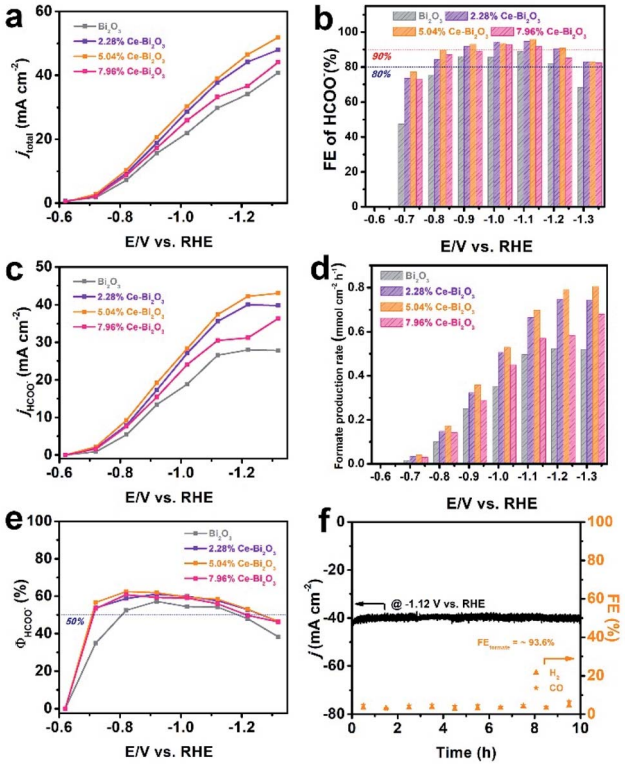

Fig. 2 (a) Total current densities, (b) potential-dependent FE for formate, (c) formate partial current densities, (d) formate production rate and (e) energy efficiency for formate for the four samples. (f) Long-term chronoamperometry test of 5.04% Ce-doped Bi_2O_3 NSs at potentials of −1.12 V, and corresponding FEs for H_2 and CO.

Bi_2O_3 NSs show the highest current density, indicating the best performance for ECR. Moreover, 5.04% Ce-doped Bi_2O_3 NSs exhibit the highest FE for formate (Fig. 2b), achieving a maximum FE value of 95.8% at −1.12 V *versus* RHE. In addition, the formate FE stably remains at about 90% in a wide negative potential range of 400 mV (from −0.82 to −1.12 V). It should be noted that H_2 FEs decrease significantly after doping Ce in Bi_2O_3 NSs (Fig. S10†), which demonstrates that doping Ce in Bi_2O_3 NSs is helpful to suppress the competing reaction of the HER. Fig. 2c and d show the formate partial current density (j_{HCOO^-}) and formate production rate of these four electrocatalysts at various potentials, respectively. Obviously, all three Ce-doped Bi_2O_3 NSs exhibit the higher j_{HCOO^-} and faster formate production rate at all potentials compared with the undoped one. In particular, 5.04% Ce-doped Bi_2O_3 NSs achieved a j_{HCOO^-} of 43.1 mA cm^{-2} and a formate production rate of 0.805 mmol cm^{-2} h^{-1} at −1.32 V, which were 1.55 times as high as those of undoped Bi_2O_3 NSs (27.8 mA cm^{-2} and 0.520 mmol cm^{-2} h^{-1}). Fig. 2e shows the energy efficiency for formate (Φ_{HCOO^-}) of the four electrocatalysts at different applied potentials. After Ce doping, the Φ_{HCOO^-} of Ce-doped Bi_2O_3 NSs increases significantly compared with that of undoped Bi_2O_3 NSs. The Φ_{HCOO^-} of 5.04% Ce-doped Bi_2O_3 NSs exceeded 50% at potentials ranging from −0.72 to −1.22 V, while that of undoped Bi_2O_3 NSs is −0.82 to −1.12 V. To the best of our knowledge, the ECR performance of 5.04% Ce-doped Bi_2O_3 NSs outperforms many other reported electrocatalysts in the H-cell (Table S1†).

The stability of 5.04% Ce-doped Bi_2O_3 NSs is tested through a long-term chronoamperometry test at −1.12 V. As shown in Fig. 2f, the current density and FE of H_2 and CO have no obvious change over 10 h of electrolysis, demonstrating the favorable stability of the electrocatalyst. The initial current density was 42.1 mA cm^{-2}, and the final current density was 40.2 mA cm^{-2}, a drop of less than 5%. The average FE of formate during 10 h reached ~93.6%, suggesting that the ECR selectivity was well maintained. After electrolysis, the morphology of 5.04% Ce-doped Bi_2O_3 NSs is largely preserved (Fig. S11a†). In addition, unavoidable reduction of Bi_2O_3 to metallic Bi happens during electrolysis, as evidenced by the XRD pattern (Fig. S11b†). This phenomenon has been reported in other studies on Bi_2O_3-based electrocatalysts as well.[47–49] Consequently, Ce-doped Bi_2O_3 NSs have high durability and selectivity towards formate generation in ECR.

To explore the factors for the enhanced electrocatalytic ability of Ce-doped Bi_2O_3 NSs, some measurements together with DFT calculations were performed. As shown in Fig. 3a, 5.04% Ce-doped Bi_2O_3 NSs possess better CO_2 adsorption capacity compared with the undoped one, which could improve the intermediate CO_2^{*-} formation before further reduction. To

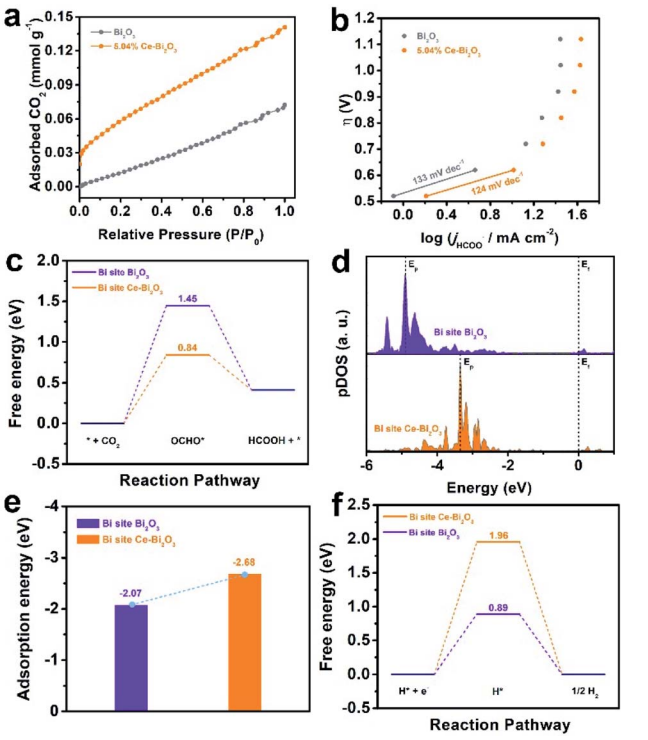

Fig. 3 (a) CO_2 adsorption isotherm and (b) Tafel plots for undoped Bi_2O_3 NSs and 5.04% Ce-doped Bi_2O_3 NSs. (c) Calculated free-energy diagram of the OCHO* intermediate, (d) projected p-orbital DOS of OCHO*, (e) calculated adsorption energy of OCHO*, and (f) calculated free-energy diagram of H* for the Bi site on Bi_2O_3 and Ce-doped Bi_2O_3.

gain deeper insight into the kinetic mechanism for ECR, the corresponding Tafel slope is fitted (Fig. 3b), which is an indicator of the rate-determining step (RDS). Obviously, the Tafel slopes for both electrocatalysts are close to the theoretical value of 118 mV dec^{-1}, suggesting that the first electron transfer process is the rate-determining step (RDS).[50,51] Furthermore, 5.04% Ce-doped Bi_2O_3 NSs exhibited a lower Tafel slope of 124 mV dec^{-1} than that of undoped Bi_2O_3 NSs (133 mV dec^{-1}), implying its better performance for ECR. Moreover, the electrochemical surface area (ECSA) of these catalysts was measured (Fig. S12†), and Ce-doped Bi_2O_3 NSs exhibited a little larger slope than that of undoped Bi_2O_3 NSs (Fig. S13†). This result suggests a slightly increased number of electrochemical active sites originating from doping Ce. These samples' activity normalized to the ECSA (the value of C_{dl}) is further calculated (Fig. S14†), which reveals that Ce-doped Bi_2O_3 NSs show its intrinsically better electrocatalytic activity for ECR.

DFT calculations are also employed to explore the origin of enhanced ECR activity of doping Ce in Bi_2O_3 NSs (calculation details are shown in the ESI, and the simulation models of undoped Bi_2O_3 and Ce-doped Bi_2O_3 are shown in Fig. S15†). Fig. 3c shows the free energy diagrams for the conversion of CO_2 to OCHO* and eventually HCOOH over the Bi-site on the undoped Bi_2O_3 and Ce-doped Bi_2O_3. Both undoped Bi_2O_3 and Ce-doped Bi_2O_3 show the largest energy barrier for OCHO* formation, demonstrating that the initial proton-coupled electron transfer is the potential limiting step. Encouragingly, after doping Ce, the energy barrier for OCHO* formation decreases from 1.45 eV for undoped Bi_2O_3 to 0.84 eV for Ce-doped Bi_2O_3. That is, it is easier to form the OCHO* intermediate on the surface of Ce-doped Bi_2O_3 compared to undoped Bi_2O_3. Besides, p-projected density of states (pDOS) analysis is shown in Fig. 3d. After OCHO* adsorption, compared with that of undoped Bi_2O_3, the highest peak of total DOS (E_p) for Ce-doped Bi_2O_3 is much closer to the Fermi level (E_f), indicating a higher binding strength of Ce-doped Bi_2O_3 to OCHO*.[52,53] Additionally, the adsorption energy of OCHO* on the electrocatalysts' surface was further studied (Fig. 3e). The adsorption energy of OCHO* on Ce-doped Bi_2O_3 was more negative than that on undoped Bi_2O_3. This result demonstrates that OCHO* adsorption on the surface of Ce-doped Bi_2O_3 is more energetically favorable than that on undoped Bi_2O_3, which coincides with the calculation results of pDOS analysis. Meanwhile, the free energies of H*on both electrocatalysts are calculated and shown in Fig. 3f. It is revealed that Ce-doped Bi_2O_3 possesses a higher energy barrier than the undoped one, indicating that Ce-doped Bi_2O_3 has lower activities toward H_2 production. Taken together, the origin of improved activity in Ce-doped Bi_2O_3 NSs can be attributed to the significant synergistic effect caused by doping Ce in Bi_2O_3, that is, the promotion of formation and adsorption of the OCHO* intermediate for ECR and depression of the formation of H* leading to suppression of the HER.

As a step further, we pursued AA-size alkaline battery-driven CO_2/H_2O splitting to explore practical application. A commercial DSA was employed as the anode for the oxygen evolution reaction (OER). The commercial DSA used here consists of a thin IrO_2 layer coated on Ta-coated-Ti foil, and it was chosen

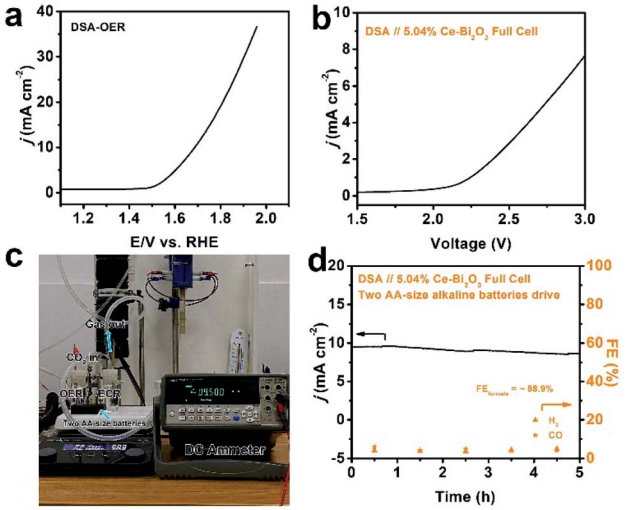

Fig. 4 Full-cell electrolysis by coupling 5.04% Ce-doped Bi_2O_3 NSs ECR with the DSA OER: (a) OER polarization curve of DSA in 0.5 M $KHCO_3$, (b) polarization curve for the ECR-OER full-cell electrolysis, (c) photograph of the setup of two AA-size alkaline batteries driving ECR-OER electrolysis and (d) current evolution and corresponding FEs of H_2 and CO for the battery-powered ECR-OER electrolysis.

as the benchmark material to couple with 5.04% Ce-doped Bi_2O_3 NS ECR. Its OER polarization curve was first collected using the standard three-electrode setup and is shown in Fig. 4a. Obviously, the anodic current density reaches 10 mA cm^{-2} at ~1.7 V in 0.5 M $KHCO_3$ electrolyte, which shows a decent OER activity. Full cells were then constructed by pairing the 5.04% Ce-doped Bi_2O_3 NS cathode and DSA anode in a two-compartment cell, and the corresponding typical polarization curve is depicted in Fig. 4b. The ECR-OER couple became turned on under an external voltage of ~2.1 V and was found to achieve a current density of 7.6 mA cm^{-2} at 3 V. Furthermore, two AA-size alkaline batteries in series were used as the power source (with an open-circuit potential of ~3.1 V) to drive the full-cell CO_2/H_2O splitting (Fig. 4c). A source-meter was connected to continuously monitor the current evolution. The current density starts at 9.5 mA cm^{-2}, slightly decreases and stabilizes at 8.5 mA cm^{-2} till the end of the 5 h evaluation (Fig. 4d). Analysis of the reduction product shows that the average formate FE is 88.9%, and the FEs of H_2 and CO are also stable. The current density of the device is relatively low because the potential on the cathode is not negative enough. If the external power source can be designed properly, the practical feasibility for the ECR-OER device will be further improved.

Conclusions

In summary, we constructed a series of Ce-doped Bi_2O_3 NS electrocatalysts with different atomic percentages of Ce through a facile solvothermal approach. The 5.04% Ce-doped Bi_2O_3 NSs possess superior activity and selectivity for CO_2 electroreduction to formate in aqueous solution. They exhibited a current density of 37.4 mA cm^{-2} with a high FE of 95.8% for formate at −1.12 V, and the formate FE was stably maintained at about 90% in

a wide potential range from −0.82 V to −1.22 V. Furthermore, some measurements together with DFT calculations were performed to explore the factors for the enhanced electrocatalytic ability. Our work demonstrates a facile doping strategy to fabricate novel Bi-based electrocatalysts, and we expect that this study can be extended to other types of highly efficient electrocatalysts for ECR.

Conflicts of interest

The authors declare that they have no conflict of interest.

Acknowledgements

The work on electron microscopy was carried out in the Center for Electron Microscopy of Zhejiang University. This work was supported by the National Science Foundation of China (51871200), National Program for Support of Top-notch Young Professionals, National Key R&D Program of China (2018YFB2200102), and Foundation for Innovative Research Groups of the National Natural Science Foundation of China (61721005).

Notes and references

1 M. Reichstein, M. Bahn, P. Ciais, D. Frank, M. D. Mahecha, S. I. Seneviratne, J. Zscheischler, C. Beer, N. Buchmann, D. C. Frank, D. Papale, A. Rammig, P. Smith, K. Thonicke, M. van der Velde, S. Vicca, A. Walz and M. Wattenbach, *Nature*, 2013, **500**, 287–295.
2 Z. Sun, T. Ma, H. Tao, Q. Fan and B. Han, *Chem*, 2017, **3**, 560–587.
3 J. Qiao, Y. Liu, F. Hong and J. Zhang, *Chem. Soc. Rev.*, 2014, **43**, 631–675.
4 E. V. Kondratenko, G. Mul, J. Baltrusaitis, G. O. Larrazábal and J. Pérez-Ramírez, *Energy Environ. Sci.*, 2013, **6**, 3112–3135.
5 Q. Wang, Y. Lei, D. Wang and Y. Li, *Energy Environ. Sci.*, 2019, **12**, 1730–1750.
6 W. Wang, S. Wang, X. Ma and J. Gong, *Chem. Soc. Rev.*, 2011, **40**, 3703–3727.
7 J. L. White, M. F. Baruch, J. E. Pander, Y. Hu, I. C. Fortmeyer, J. E. Park, T. Zhang, K. Liao, J. Gu, Y. Yan, T. W. Shaw, E. Abelev and A. B. Bocarsly, *Chem. Rev.*, 2015, **115**, 12888–12935.
8 J. Shi, Y. Jiang, Z. Jiang, X. Wang, X. Wang, S. Zhang, P. Han and C. Yang, *Chem. Soc. Rev.*, 2015, **44**, 5981.
9 L. Zhang, Z. Zhao, T. Wang and J. Gong, *Chem. Soc. Rev.*, 2018, **47**, 5423.
10 M. G. Kibria, J. P. Edwards, C. M. Gabardo, C. Dinh, A. Seifitokaldani, D. Sinton and E. H. Sargent, *Adv. Mater.*, 2019, **31**, 1807166.
11 L. Zhang, Z. Zhao and J. Gong, *Angew. Chem., Int. Ed.*, 2017, **56**, 11326–11353.
12 C. Long, X. Li, J. Guo, Y. Shi, S. Liu and Z. Tang, *Small Methods*, 2019, **3**, 1800369.
13 Y. Quan, J. Zhu and G. Zheng, *Small Sci.*, 2021, **1**, 2100043.
14 J. Li, Y. Kuang, Y. Meng, X. Tian, W. Hung, X. Zhang, A. Li, M. Xu, W. Zhou, C. Ku, C. Chiang, G. Zhu, J. Guo, X. Sun and H. Dai, *J. Am. Chem. Soc.*, 2020, **142**, 7276–7282.
15 N. Han, P. Ding, L. He, Y. Li and Y. Li, *Adv. Energy Mater.*, 2019, **10**, 1902338.
16 S. Enthaler, J. von Langermann and T. Schmidt, *Energy Environ. Sci.*, 2010, **3**, 1207–1217.
17 W. Wang, Y. Himeda, J. T. Muckerman, G. F. Manbeck and E. Fujita, *Chem. Rev.*, 2015, **115**, 12936–12973.
18 L. Fan, C. Xia, P. Zhu, Y. Lu and H. Wang, *Nat. Commun.*, 2020, **11**, 3633.
19 M. G. Mura, L. D. Luca, G. Giacomelli and A. Porcheddu, *Adv. Synth. Catal.*, 2012, **354**, 3180–3186.
20 P. Ding, H. Zhao, T. Li, Y. Luo, G. Fan, G. Chen, S. Gao, X. Shi, S. Lu and X. Sun, *J. Mater. Chem. A*, 2020, **8**, 21947–21960.
21 Y. Zhou, R. Zhou, X. Zhu, N. Han, B. Song, T. Liu, G. Hu, Y. Li, J. Lu and Y. Li, *Adv. Mater.*, 2020, **32**, 2000992.
22 Z. Li, A. Cao, Q. Zheng, Y. Fu, T. Wang, K. T. Arul, J. Chen, B. Yang, N. M. Adli, L. Lei, C. Dong, J. Xiao, G. Wu and Y. Hou, *Adv. Mater.*, 2020, **33**, 2005113.
23 Z. Zhang, F. Ahmad, W. Zhao, W. Yan, W. Zhang, H. Huang, C. Ma and J. Zeng, *Nano Lett.*, 2019, **19**, 4029–4034.
24 J. Zhu, J. Fan, T. Cheng, M. Cao, Z. Sun, R. Zhou, L. Huang, D. Wang, Y. Li and Y. Wu, *Nano Energy*, 2020, **75**, 104939.
25 Y. Qiao, W. Lai, K. Huang, T. Yu, Q. Wang, L. Gao, Z. Yang, Z. Ma, T. Sun, M. Liu, C. Lian and H. Huang, *ACS Catal.*, 2022, **12**, 2357–2364.
26 F. Yang, A. O. Elnabawy, R. Schimmenti, P. Song, J. Wang, Z. Peng, S. Yao, R. Deng, S. Song, Y. Lin, M. Mavrikakis and W. Xu, *Nat. Commun.*, 2020, **11**, 1088.
27 N. Han, Y. Wang, H. Yang, J. Deng, J. Wu, Y. Li and Y. Li, *Nat. Commun.*, 2018, **9**, 1088.
28 X. Zhang, X. Sun, S. Guo, A. M. Bond and J. Zhang, *Energy Environ. Sci.*, 2019, **12**, 1334–1340.
29 Z. Zhang, M. Chi, G. M. Veith, P. Zhang, D. A. Lutterman, J. Rosenthal, S. H. Overbury, S. Dai and H. Zhu, *ACS Catal.*, 2016, **6**, 6255–6264.
30 H. Xie, T. Zhang, R. Xie, Z. Hou, X. Ji, Y. Pang, S. Chen, M. Titirici, H. Weng and G. Chai, *Adv. Mater.*, 2021, **33**, 2008373.
31 J. Fan, X. Zhao, X. Mao, J. Xu, N. Han, H. Yang, B. Pan, Y. Li, L. Wang and Y. Li, *Adv. Mater.*, 2021, **33**, 2100910.
32 Y. Duan, K. Liu, Q. Zhang, J. Yan and Q. Jiang, *Small Methods*, 2020, **4**, 1900846.
33 Z. Chen, K. Mou, X. Wang and L. Liu, *Angew. Chem., Int. Ed.*, 2018, **57**, 12790–12794.
34 Q. Lia, X. Zhang, X. Zhou, Q. Li, H. Wang, J. Yi, Y. Liu and J. Zhang, *J. CO2 Util.*, 2020, **37**, 106–112.
35 S. Liu, X. Lu, J. Xiao, X. Wang and X. W. Lou, *Angew. Chem., Int. Ed.*, 2019, **58**, 13828–13833.
36 F. Meng, Q. Zhang, K. Liu and X. Zhang, *Chem.–Eur. J.*, 2020, **26**, 4013–4018.
37 X. Li, X. Wu, J. Li, J. Huang, L. Ji, Z. Leng, N. Qian, D. Yang and H. Zhang, *Nanoscale*, 2021, **13**, 19610–19616.

38 Y. Zhao, X. Liu, Z. Liu, X. Lin, J. Lan, Y. Zhang, Y. Lu, M. Peng, T. Chan and Y. Tan, *Nano Lett.*, 2021, **21**, 6907–6913.
39 S. Liu, M. Gao, R. Feng, L. Gong, H. Zeng and J. Luo, *ACS Catal.*, 2021, **11**, 7604–7612.
40 X. Chen, H. Chen, W. Zhou, Q. Zhang, Z. Yang, Z. Li, F. Yang, D. Wang, J. Ye and L. Liu, *Small*, 2021, **17**, 2101128.
41 Y. Duan, Y. Zhou, Z. Yu, D. Liu, Z. Wen, J. Yan and Q. Jiang, *Angew. Chem., Int. Ed.*, 2021, **60**, 8798–8802.
42 R. Pang, P. Tian, H. Jiang, M. Zhu, X. Su, Y. Wang, X. Yang, Y. Zhu, L. Song and C. Li, *Natl. Sci. Rev.*, 2021, **8**, nwaa187.
43 S. B. Varandili, J. Huang, E. Oveisi, G. L. D. Gregorio, M. Mensi, M. Strach, J. Vavra, C. Gadiyar, A. Bhowmik and R. Buonsanti, *ACS Catal.*, 2019, **9**, 5035–5046.
44 H. Dong, L. Zhang, L. Li, W. Deng, C. Hu, Z. Zhao and J. Gong, *Small*, 2019, **15**, 1900289.
45 S. Ning, Z. Guo, J. Wang, S. Huang, S. Chen and X. Kang, *ChemElectroChem*, 2021, **8**, 2680–2685.
46 S. Li, D. Bao, M. Shi, B. Wulan, J. Yan and Q. Jiang, *Adv. Mater.*, 2017, **29**, 1700001.
47 D. Wu, G. Huo, W. Chen, X. Fu and J. Luo, *Appl. Catal., B*, 2020, **271**, 118957.
48 Q. Gong, P. Ding, M. Xu, X. Zhu, M. Wang, J. Deng, Q. Ma, N. Han, Y. Zhu, J. Lu, Z. Feng, Y. Li, W. Zhou and Y. Li, *Nat. Commun.*, 2019, **10**, 2807.
49 C. W. Lee, J. S. Hong, K. Yang, K. Jin, J. H. Lee, H. Y. Ahn, H. Seo, N. E. Sung and K. T. Nam, *ACS Catal.*, 2018, **8**, 931–937.
50 D. Zhu, J. Liu and S. Qiao, *Adv. Mater.*, 2016, **28**, 3423–3452.
51 Y. Duan, F. Meng, K. Liu, S. Yi, S. Li, J. Yan and Q. Jiang, *Adv. Mater.*, 2018, **30**, 1706194.
52 Z. Chen, X. Zhang, M. Jiao, K. Mou, X. Zhang and L. Liu, *Adv. Energy Mater.*, 2020, **10**, 1903664.
53 B. Hammer and J. K. Nørskov, *Surf. Sci.*, 1995, **343**, 211–220.